J. Fluid Mech. (1977), *vol.* 80, *part* 4, *pp.* 617–640
Printed in Great Britain

Cavitation noise and inception as influenced by boundary-layer development on a hydrofoil

By WILLIAM K. BLAKE, M. J. WOLPERT AND F. E. GEIB

Naval Ship Research and Development Center, Department of the Navy, Bethesda, Maryland 20084

(Received 4 December 1975)

This paper describes measurements of noise from two-phase flow over hydrofoils. The experiments were performed in a variable-pressure water tunnel which was acoustically calibrated so that sound power levels could be deduced from the sound measurements. It is partially reverberant in the frequency range of interest.

Cavitation was generated on a hydrofoil in the presence of either a separated laminar boundary layer or a fully turbulent attached boundary layer. The turbulent boundary layer was formed downstream of a trip which was positioned near the leading edge. High-speed photographs show the patterns of cavitation which were obtained in each case. The noise is shown to depend on the type of cavitation produced; and for each type, the dependence on speed and cavitation index has been determined. Dimensionless spectral densities of the sound are shown for each type of flow.

1. Introduction

Very few quantitative measurements of noise from surface cavitation on hydrofoils have been reported. Often such measurements were relative to some arbitrary level and they have not always been supported by the observation of additional parameters which may influence the interpretation of the data. Factors which can affect this interpretation include acoustic absorption and reverberation in the test chamber, the proximity of the receiver to the cavitation, and hydrodynamic factors that control the type, extent and inception of the cavitation.

In the investigations discussed in this paper an effort has been made to provide coincident acoustic and hydrodynamic observations of hydrofoil cavitation. Measurements were made of the noise from a hydrofoil on which the boundary layer was either tripped to turbulence or not tripped and still laminar. It was seen that viscous effects on the types of cavitation existing were responsible for differing observed cavitation dynamics and differing noise characteristics.

Section 2 of the paper describes the instrumentation. The non-cavitating boundary-layer characteristics and the effectiveness of a leading-edge trip in eliminating laminar separation are discussed in § 3. In § 4 the measured influences of the boundary layer on the type of cavitation and of free gas on the inception of each type are described and related to recent observations on axisymmetric head-forms. In § 5 the results of high-speed motion photography of the two types of cavitation observed in this study are

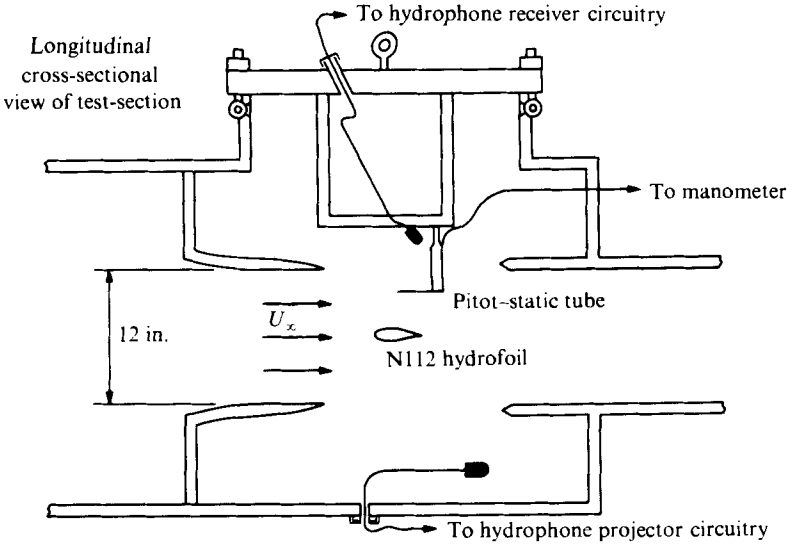

FIGURE 1. Diagram of the experimental arrangement in the 12 in. variable-pressure water tunnel.

reviewed. Sections 6 and 7 are concerned with the noise of each type and with the scaling of the cavitation noise. A more complete account of the investigation is given by Blake *et al* (1976).

2. Description of foil and experimental technique

General considerations

Cavitation measurements were carried out in the David W. Taylor Naval Ship Research and Development Center (DTNSRDC) 12 in. variable-pressure water tunnel, which is of the open-jet type and is equipped with a deaeration system, but not a resorber. The hydrofoil used for the experiments had a 4 in. chord, was made of brass according to a design by Liebeck (1973) of McDonnell-Douglas Aircraft Corporation and was designated as N112. This particular hydrofoil shape was selected for the chordwise extent of low pressure, which was expected to produce well-defined cavitation patterns away from the leading edge of the hydrofoil. The surface co-ordinates and the theoretical pressure coefficients for the N112 hydrofoil were calculated subject to an imposed condition of avoiding turbulent boundary-layer separation at a specified Reynolds number. However, after the design had been completed a smaller chord of 4 in. was selected for use as the largest which would yield sufficiently small tunnel jet deflexions and a sufficiently large aspect ratio (approximately 2:1 in the jet). Operation at a lower Reynolds number than the design condition resulted in the occurrence of a laminar boundary layer on the 'low pressure' side rather than the turbulent boundary layer for which the hydrofoil was designed. Without tripping, the laminar boundary layer separated downstream of the minimum pressure point on the hydrofoil. The hydrofoil spanned the test section horizontally and was supported by stainless-steel bars which penetrated the tunnel viewing ports; its angle of attack was continuously variable. The free-stream water pressure was measured with a closed-end mercury manometer connected to the static pressure tap of a Pitot–static tube mounted

approximately 3 in. above the hydrofoil as illustrated in figure 1. The water temperature was monitored on a thermometer immersed in the test section. The air content was determined by means of a Yellow Springs Instrument Company 'Dissolved Oxygen Meter', Model Number 51A, which directly measures dissolved oxygen. The dissolved oxygen content was interpreted as a percentage of the dissolved gas at saturation in equilibrium with air at one atmosphere. These values of equivalent air content obtained with the dissolved oxygen meter were within 1 % of the saturation content of those directly measured with the van Slyke blood gas apparatus.

Noise measurement equipment

Sound pressure levels (SPL) in the water tunnel were measured using a KSP Industries Model UT-112 hydrophone modified for use in a low pressure environment. The hydrophone was mounted on an angle-iron support about 9 in. above the hydrofoil (see figure 1), just outside the free shear layer of the water jet. For all measurements the amplified hydrophone output was frequency analysed with a General Radio Model 1925/1926 $\frac{1}{3}$-octave band filter and detector combination. A second hydrophone was permanently installed in the tunnel outside the water jet at the end of the hydrofoil for use as a reference sound projector. It was excited by filtered random noise when desired. Cavitation noise measurements were made with a 32 s averaging time.

Effects of test-section reverberation, absorption and hydrofoil vibration

Estimated free-field sound levels were the goal of the cavitation noise measurement scheme of this project. The acoustic reverberation of the test section was evaluated using a KSP Industries UT-111 hydrophone as an acoustic volume source. Both the receiver and the projector were previously calibrated in the free-field environment to determine their sensitivities and directivity factors. In the water-tunnel test section the projector was driven with random noise and placed at locations where cavitation would occur. For each location, the broad-band noise was received at the location used in the measurement of cavitation noise. This was a distance of 9 in. above the suction side of the hydrofoil. The ratio of the measurements in the water tunnel to those taken in the free field at a 1 yd acoustic range gave the corrections to be applied to all cavitation noise measurements so that 1 yd source levels could be estimated. Actually the measurements were made within one acoustic wavelength of the hydrofoil for frequencies less than 6000 Hz. The procedure used in the reverberation investigation was expected to account for corrections due to any tunnel acoustic resonances which might have existed. Figure 2 shows ratios of sound levels measured in the tunnel at a 9 in. source–receiver separation to the free-field source levels measured at 1 yd separation. These ratios were used to calculate the effective free-field cavitation noise levels reported in this paper. These levels are approximate for frequencies less than 6000 Hz.

The hydrophone projector mounted outside the flow at one end of the hydrofoil during noise measurements was used to monitor the acoustic absorption in the test section, which was caused by the formation of free-gas bubbles. These bubbles could be formed during the operation of the test section at low pressure for extended periods of time. Absorption of sound by these bubbles would occur at their resonance frequencies; it was quantitatively established by monitoring the sound levels generated at the receiving hydrophone by the acoustic projector mounted at the end of the

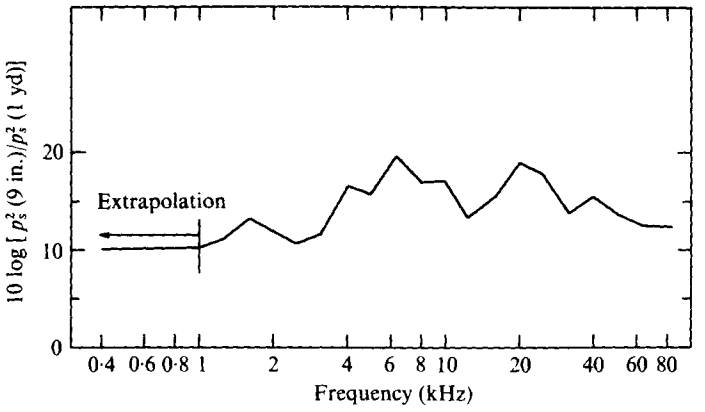

FIGURE 2. Test-section acoustic calibration expressed as ratio of mean-square pressure 9 in. from the source in the tunnel to that measured at 1 yd in a free field.

hydrofoil. At any static pressure of the test section, with or without cavitation on the hydrofoil, this source could be used to ensonify the water tunnel. Reductions in received noise level for a standard powering voltage applied to the source were interpreted as indicating the presence of small gas bubbles in the water tunnel. The source used in this measurement was of the same type as that used to acoustically calibrate the water tunnel; it was capable of producing noise levels in excess of those generated by the cavitation. Received noise levels at atmospheric pressure and with deaerated water were used to set a standard for noise levels in the test section which were not influenced by absorption due to suspended gas bubbles. The maintenance of these levels at low pressures, say $\frac{1}{5}$ atm, in the test section was considered to be indicative that free-gas bubbles were still absent either with or without cavitation. Acoustic absorption of 1 dB, as determined by received noise levels being less than those regarded as standard, was sufficient to cause the termination of the test. There was no measurable acoustic absorption due to the cavitation on the hydrofoil. This method of monitoring free gas could be used as a reliable way to detect bubbles, but it could not be used to quantify free-gas concentration, because loss factors for bubbles are not known with the required certainty. The procedure did offer a means of establishing the presence of bubbles which could absorb sound as well as act as possible nucleation sites.

Radiation due to resonant modal excitation of the hydrofoil by the cavitation was investigated. This was accomplished indirectly by mechanically shaking the hydrofoil and measuring the acceleration levels on the foil along with received acoustic levels at the hydrophone produced by the vibration. A transfer function was obtained which consisted of frequency-dependent ratios of the radiated sound level to the acceleration averaged over the hydrofoil surface. Using the transfer function as well as coincident cavitation noise and acceleration levels during flow, it was found that noise radiated directly from cavitation exceeded the vibration-induced noise by at least 6 dB from 1 to 10 kHz (see also Blake *et al.* 1976).

Measurement procedure

The test section of the water tunnel was filled from the water main; the water received no special treatment except filtering. Following filling, the tunnel water was deaerated

for the period of time necessary to reduce the gas content to below 10 % of saturation by dissolved gas at atmospheric pressure (below approximately 50 % of saturation at the static pressure in the test section during tests). Under these conditions there was no observable acoustic absorption due to free-gas bubbles. Often the deaeration would proceed for extended periods to make use of time during which acoustic measurements were not being conducted. In spite of this repeated deaeration, continued operation with cavitation in the test section resulted in a slow accumulation of free gas (Knapp, Daily & Hammett (1970, p. 469) have discussed this accumulation in water tunnels without resorbers). The apparent dissolved gas content indicated by the oxygen meter continued to decrease with time after filling. Refilling the test section and upper duct of the water tunnel with fresh water followed by deaeration would restore the water to its test condition.

The measurement procedure involved establishing the tunnel speed for a given run, then reducing the pressure until inception was reached. The noise measurements were then conducted at continuously reduced cavitation indices ranging from slightly greater than that for inception to that required for the jet shear layer and/or collector ring to cavitate excessively or until free-gas bubbles were detected by the procedure outlined above. An acoustic absorption from the source of 1 dB usually marked the end of a test. Background levels were continuously monitored during the experiments by changing the angle of attack of the hydrofoil while maintaining a fixed cavitation index; this change reduced or eliminated the cavitation on the hydrofoil. In addition, noise was determined with the hydrofoil removed at a given free-stream cavitation index and water velocity. Background levels were generally found to be dominated by impeller cavitation for cavitation indices between approximately 3 and 0·6 and by cavitation in the shear layer of the water-tunnel jet for indices less than 0·6. The inception of shear-layer cavitation was variable, especially with time after filling. Cavitation inception indices were generally 0·6 when steady-state conditions were established some hours after a cavitation experiment commenced, but shortly after filling they were observed to be lower; at one point the index was less than 0·44. Knapp *et al.* have quoted typical values of 0·55. Background levels originating from both the shear layer and the impeller cavitation were somewhat variable. Thus the continuous monitoring of the background as described above was important.

3. Descriptions of the boundary layers on the hydrofoil

Our comments will be restricted to cavitation on side I, i.e. the theoretical low pressure side of the hydrofoil, whose cross-sectional shape is shown in figure 3. Cavitation on side II and more extensive acoustic results are described by Blake *et al.* (1976). The static pressure distribution on side I was determined by using static pressure taps at distances downstream of the leading edge of 7·5, 20, 30 and 40 % of the chord c. Figure 3 also shows the theoretical and measured pressure distributions at a 4° angle of attack. The angles of attack reported in this paper are relative to the centre-line of the tunnel. Measurements are shown as a function of speed for the tripped boundary layer and at a single speed without the trip. The coefficients give local pressures P relative to the ambient static pressure P_∞ normalized by the inflow speed U_∞. Laminar boundary-layer separation was experimentally established for non-tripped flow by performing an oil-film experiment. A mixture of lamp black and high viscosity (SAE 90) gear oil was

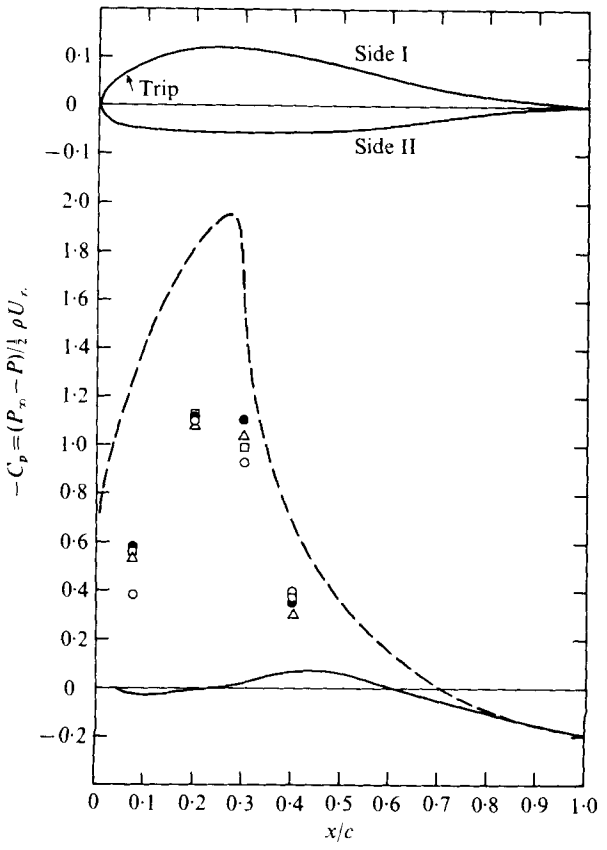

FIGURE 3. Pressure coefficients and cross-sectional shape of Liebeck N112 hydrofoil. Data and theoretical calculations are for a 4° angle of attack with tripped and untripped boundary layers on the suction side. Theoretical values (McDonnell-Douglas Corp): – – –, side I; ——, side II. Measurements, tripped: ○, 20 ft/s; □, 16 ft/s; △, 10 ft/s. Measurements, untripped: ●, 20 ft/s.

applied to the suction side of the hydrofoil, the tunnel was then filled and the water accelerated to a selected speed. The region of separation was indicated by a band of oil which remained on the hydrofoil surface. Table 1 shows the extent of the separation at a 4° angle of attack for six speeds. The spatial resolution of the oil film was within $\frac{1}{16}$ in. At 6 ft/s the separation extended to the trailing edge. From 15 ft/s to 22 ft/s it was of small chordwise extent and uniform along the entire span. At 24 ft/s the chordwise extent was only about 0·1 in and separation occurred in a broken line along the span. Patterns of similar chordwise and spanwise extents were observed an angle of attack $\alpha = 2°$.

That the free-stream turbulence in the water tunnel was insufficient to cause natural transition on the untripped hydrofoil was established using criteria of Hall & Gibbings (1972). The broad-band root-mean-square turbulence intensity on the centre-line was 2 % of the free-stream velocity. Using the equations for laminar boundary-layer growth in the absence of a pressure gradient (Schlichting 1960, p. 123), we estimated that the Reynolds number at the observed separation point was only $U_\infty \theta/\nu = 290$. The effect of the favourable pressure gradient would have been to reduce the momentum thickness θ, as well as to stabilize the laminar boundary layer further. Without the

U_∞(ft/s)	Region of separation, $\alpha = 4°$
6	$0{\cdot}25 < x/c < 1$
8	$0{\cdot}25 < x/c < 0{\cdot}55$ to $0{\cdot}75$
15	$0{\cdot}28 < x/c < 0{\cdot}35$
20	$\sim 0{\cdot}3 < x/c < \sim 0{\cdot}33$
22	$0{\cdot}3 < x/c < 0{\cdot}33$
24	$0{\cdot}3 < x/c < 0{\cdot}33$

TABLE 1. Separation region on high-lifting hydrofoils without tripping.

stabilizing influence of the pressure gradient Hall & Gibbings (1972) showed that the Reynolds number required for transition with a free-stream turbulence intensity of 1·5 % was at least $U_\infty \theta/\nu = 400$.

The boundary-layer trip was a strip of tape $\frac{1}{32}$ in. in streamwise extent with a height of $5{\cdot}6 \times 10^{-3}$ in. The trailing edge of the trip was situated approximately at $x/c = 0{\cdot}04$. The trip was designed by determining that the estimated height of the laminar boundary layer at the trip location, which was $4{\cdot}3 \times 10^{-3}$ in. at 22 ft/s, was less than the height of the trip. Its effectiveness was speed dependent. The oil-film experiment disclosed that laminar separation at $\alpha = 4°$ and 16 ft/s was intermittent; this was deduced from the rapid occurrence of a fairly well-defined accumulation of oil which gradually washed off. At higher speeds no separation could be detected on the suction side of the hydrofoil, indicating that transition to turbulence occurred upstream of the position of minimum pressure. The static pressure distributions (figure 3) reflected the speed dependence of the effectiveness of the trip in eliminating separation. At $x/c = 0{\cdot}2$ the pressure coefficients were independent of speed; at $x/c = 0{\cdot}3$ the pressure coefficients for the tripped boundary layer consistently approached that for the untripped laminar boundary layer as the speed was reduced.

The theoretical static pressure distribution for an assumed two-dimensional flow, provided by R. H. Liebeck, is also shown in figure 3. The discrepancy between the measured and the calculated distributions on side I is deduced to be due to the reduced aspect ratio of the hydrofoil in the open jet of the water tunnel. The mean velocity of the jet of the water tunnel was constant over a 9 in. diameter core, so that the effective aspect ratio of the hydrofoil was of the order of 2. An experimental examination of the boundary layer characteristics on side II of the hydrofoil was not made; nor were lift coefficients of the hydrofoil measured.

4. The characteristics of cavitation inception

This section examines the influence of the boundary layer on the type of cavitation which developed on the hydrofoil. It also discusses some effects of undissolved gas in the free stream on the inception of each type of cavitation. Incipient cavitation indices were determined by slowly lowering the tunnel pressure at constant water velocity until fully developed cavitation occurred. The definition of the onset depended on the type of cavitation which occurred. Desinent indices were determined by increasing the static pressure and noting the cessation of cavitation. In all cases the cavitation has been characterized by the index

$$\sigma = (P_\infty - P_v)/\tfrac{1}{2}\rho U_\infty^2,$$

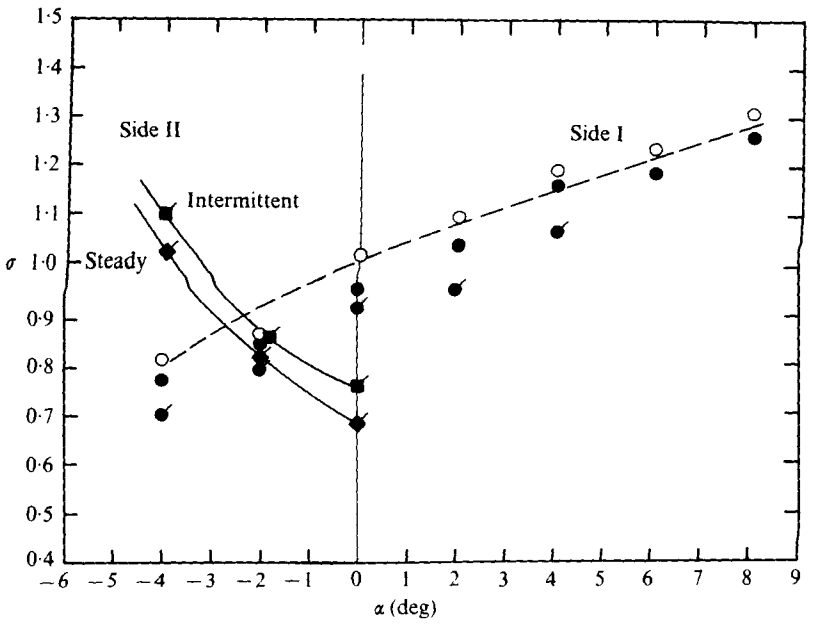

FIGURE 5. Incipient and desinent cavitation numbers for the hydrofoil with no trip shown as function of angle of attack for $U_\infty = 22$ ft/s. Air content 9 %: ○, desinent, ●, incipient. ●, ■, ▲, air content 11 %; – – –, measured values of $-C_{p\min}$.

where P_v is the vapour pressure of the water. The incipient indices are denoted by σ_i and the desinent indices by σ_d. Regardless of the type of cavitation, however, there was little difference between σ_i and σ_d. All measurements were performed with a dissolved air content of the order of 1–2·4 p.p.m. by weight, or 5–12 % of saturation at the measured water temperature and atmospheric pressure. The free-gas content, detected by acoustic absorption as described in § 2, was qualitatively observed to increase very slightly with time after filling. Although no direct quantitative dependence of σ_i on small changes in combined free and dissolved air content could be determined, inception indices increased slightly with time after filling. These increases depended on the type of cavitation which existed, and they did not exceed 15 %. Holl's (1960) equilibrium theory did not quantitatively account for observed changes in σ_i or σ_d with gas content although these parameters tended to increase with increases in either dissolved or free gas. Owing to the low dissolved gas contents in the present study compared with Holl's (1960) (2·4 compared with 27 p.p.m.), the current measurements are perhaps less likely to be influenced by dissolved gas.

Effects of the boundary-layer trip on cavitation

Cavitation which began in the vicinity of the separated laminar boundary layer, i.e. with no trip, appeared as a well-defined strip which extended chordwise downstream from $x/c \simeq 0{\cdot}25$. Figure 4 (plate 1) shows typical photographs of this type of cavitation taken under stroboscopic light with an exposure of 3×10^{-6} s. The forward edge of the cavitation is smooth in places, indicating non-turbulent flow at these locations. Downstream of the forward edge the cavity is broken up, but the high density of bubbles is still well defined over its chordwise extent. Visual observation of the cavitation showed

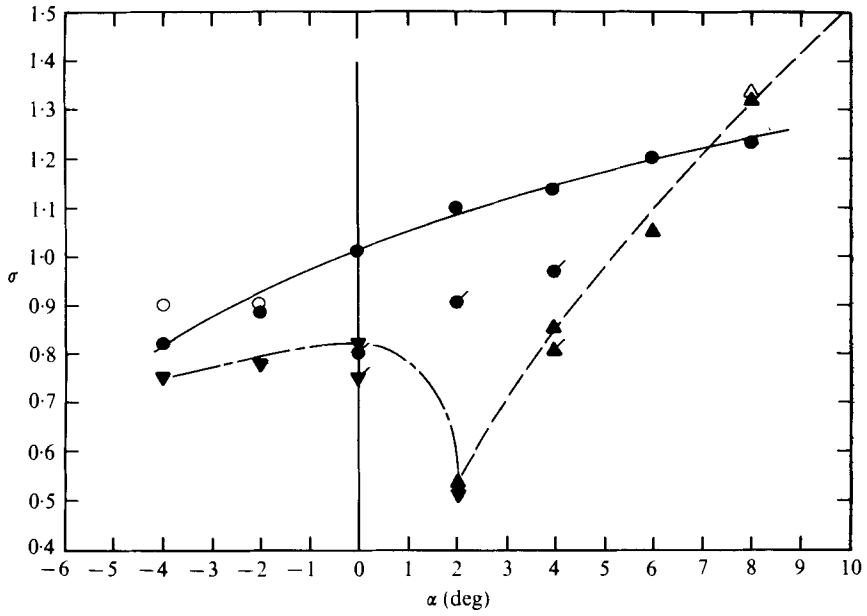

FIGURE 7. Incipient and desinent cavitation numbers for the hydrofoil with a tripped turbulent boundary layer. Inception of cavitation types on side I is shown for varying quantities of free gas; $U_\infty = 22$ ft/s. Cavitation type: ——, travelling bubble; – – –, trip induced; — — —, intermittent laminar separation. Non-flagged points indicate measurements affected by free gas. ○, incipient; ●, desinent.

that the approximate chordwise length l_c of the cavitation region appeared to be roughly proportional to $\sigma_i - \sigma$. These photographs will be discussed further in the next section.

Incipient and desinent indices are shown in figure 5. Inception was defined visually to occur when the cavitation was unsteady but present on the hydrofoil 50–80 % of the time. The data are typical of the speed range 16–22 ft/s. The flagged and unflagged points were obtained on different days separated by tunnel drainings and fillings. For the flagged points there were no free-gas bubbles as indicated by negligible acoustic absorption from the reference source, however for the unflagged points absorption of 1–2 dB occurred in the frequency range 10–100 kHz, indicating the presence of free-gas bubbles. The dashed line in figure 5 shows the variation of the measured minimum pressure coefficient with angle of attack. Actual minima of the pressure coefficient may have been as much as 10 % lower than the ones measured because the wide spacing of the static pressure taps may not have been sufficient to resolve the pressure distribution accurately. Incipient indices for pressure-side cavitation are shown for both intermittent and steady cavitation. This cavitation had the visual appearance of a steady broken sheet of bubbles extending from the leading edge and collapsing just above the surface of the hydrofoil. No further discussion will be given of pressure-side cavitation.

When cavitation began on the hydrofoil in the vicinity of an attached (tripped) turbulent boundary layer, the visual appearance of the cavitation was that of white streaks passing over the region of low pressure on the hydrofoil, roughly

$$0{\cdot}15 < x/c < 0{\cdot}90.$$

Figure 6 (plate 2) is a stroboscopic photograph of this cavitation at $\sigma = 0{\cdot}78$, showing that the white streaks were comprised of discrete bubbles having a wide range of sizes and shapes. These photographs will be further discussed in § 5. The incipient and desinent indices for this cavitation on the hydrofoil are shown in figure 7. In contrast to the 'on and off' incipient cavitation discussed above, the inception of this type of cavitation was detectable as a sequence of clearly distinguishable audible and visible 'events' of short time duration. As the static pressure was reduced the event rate increased as the cavitation generated steady-state random noise. Incipient event-counting was accomplished audibly using a wrist watch while observing the cavitation for 30 s. Two sets of incipient indices appear in the figure: these are the results of separate measurements on different days. The first set, denoted by the unflagged points, was measured during a period when a small air leak in the tunnel brought about a slow accumulation of free gas causing 1–2 dB absorption of noise generated by the reference source. These inception points were established on the basis of the first audible event. The second set of indices was obtained on another day with the leak repaired, using a steady event rate of 1–2 s^{-1}. The dissolved air content was 8 % of saturation at the tunnel temperature and atmospheric pressure for both sets of measurements.

The uncertainty in σ_i caused by the different event-rate criteria is approximately 6 %, so that the 20 % difference in the incipient indices in figure 7 is largely due to the populations of free-gas bubbles, indicated by the absorption of sound from the reference source. The lower inception indices, accompanying lower free-gas contents, are consistent with the results of other investigations, e.g. Peterson (1969) and Brockett (1972). The acoustic absorption at $\frac{1}{5}$ atm often observed in this study at 50 kHz required the resonant excitation of suspended bubbles with radii of the order of 3×10^{-3} cm. Although 1–2 dB absorption in this frequency range was the maximum tolerated for the current measurements, these and smaller bubbles were obviously present in the tunnel. Furthermore, Peterson (1972) has holographically measured stable bubbles with radii of the order of 10^{-3} cm in the facility used for this investigation, but at a slightly higher static pressure than that used in the current measurements. Strasberg (1956) has shown that the critical pressure for cavitation is a function of both the nucleus bubble radius and the free-gas content. Decreasing the gas-nucleus (bubble) sizes and decreasing the undissolved concentrations caused a marked decrease in critical pressure. Therefore it is reasonable to expect that when, in the current experiments, no absorption existed below 50 kHz all gas-filled nuclei were less than 10^{-3} cm in radius and became available in increasing numbers as the static pressure in the water tunnel was reduced.

Further reduction in the static pressure in the tunnel resulted in the first occurrence of cavitation on the boundary-layer trip at $\sigma = 0{\cdot}85$ and $\alpha = 4°$. At this index the trip cavitation was very intermittent, occurring at long time intervals and often at one location along the span. This indicated that a slight spatial non-uniformity in the trip shape caused the cavitation. The cavitation of three-dimensional triangular protuberances, which typify local pointed elements on a hydrofoil, has been examined by Holl, Arndt & Billet (1972). Use of the estimated boundary-layer characteristics at the trip location on the present hydrofoil resulted in an estimate of $\sigma_i \simeq 0{\cdot}67$. At larger angles of attack the cavitation on the hydrofoil became totally dominated by the trip. On the other hand, for $\alpha < 2°$ the trip-induced cavitation became non-existent, but an intermittent type, typical of that associated with laminar separation on the untripped

α	U_∞ (ft/s)	No trip	Trip	$-C_{p\min}$ (measured)
4°	18	1·09	0·90	1·13
4°	22	1·02	0·90	1·13
2°	22	0·95	0·86	1·05
0	22	0·92	0·80	0·96

TABLE 2. Comparison of tripped σ_i with non-tripped σ_i for Liebeck N112 Hydrofoil, 2·2 p.p.m.w. air content (1–2 events/s).

hydrofoil, became apparent. For increasingly negative angles of attack, the cavitation associated with laminar boundary-layer separation soon followed the inception of travelling-bubble cavitation on the hydrofoil. Apparently the effectiveness of the boundary-layer trip diminished and the boundary layer in the zone of minimum pressure become laminar as the angle of attack on the hydrofoil became negative. Comparisons of the values of σ_i for cavitation related to laminar separation in figures 5 and 7 show that at $\alpha = -4°$ the cavitation characteristics of the tripped and untripped hydrofoils were comparable.

Viscous effects on inception

Viscous effects on cavitation inception for axisymmetric head-forms have been discussed by Peterson (1969) and observed by Arakeri & Acosta (1973) and Acosta (1974). When laminar boundary-layer separation occurs, cavitation indices have been observed to be higher than when separation is prevented. In this connexion, Casey (1974) has quantitatively related experimentally observed values of σ_i to computed static pressure coefficients on a hydrofoil at flow separation. He has also correlated the observed location of the cavitation with the observed location of laminar boundary-layer separation. In the current experiment, a relationship between the occurrence of laminar flow separation and the inception and type of cavitation has also been observed. Laminar separation occurred slightly downstream of but still near the point of minimum measured pressure coefficient $C_{p\min}$, and the cavitation was entirely downstream of that point. This can be seen by reference to figure 8 (plate 3), which compares the measured pressure distributions with photographs of the incipient cavitation. The downstream extremity of the region of laminar separation can be seen to coincide with the location of small bubbles. The dynamics of the cavitation, as disclosed by the high-speed motion photography described in § 5, were clearly seen to be initiated by the formation of these small bubbles. Thus inception appeared to occur at the reattachment point. This is in agreement with the head-form observations of Arakeri & Acosta (1973), which showed bubbles to be formed in this region. The generally lower σ_i for travelling-bubble cavitation on the tripped hydrofoil compared with the untripped cases can be seen by reference to table 2. Well-developed steady-state bound cavitation occurred at 10 % higher σ when laminar separation occurred than when it was suppressed by tripping.

The data in table 2 were generated within a single day at the same time as the flagged points of figures 5 and 7 with a single tunnel filling. These data correspond to flow immediately before and after removal of the trip so they are not influenced by uncertainties caused by time-dependent free-gas accumulation. The occurrence of the

occasional audible events associated with $\sigma > \sigma_i$ for travelling bubbles is most probably due to local pressure fluctuations in the turbulent boundary layer of the hydrofoil which have a small but finite probability of being less than the critical pressure required for bubble growth. The occurrence of inception at a higher σ for a case involving laminar separation than for cases with attached boundary-layer flow has been attributed by Arakeri & Acosta (1973) to extraordinarily high wall pressure fluctuations occurring at the reattachment point. Arakeri (1974) has observed that these fluctuations are considerably higher than when separation is suppressed; broad-band fluctuations extending to 10 % of the dynamic head were observed on a hemispherical nose. In the case of a two-dimensional strut, pressure fluctuations of the order of 18 % of the free-stream dynamic head were observed (in connexion with another experiment; Blake 1975) in the reattachment region of the separated flow downstream of a circular leading edge. Pressure fluctuations in the fully developed turbulent boundary-layer flow just downstream of the reattachment zone on the same strut were a factor of 10 less than those associated with separation. Additional evidence of the role of local pressure (and velocity) fluctuations in causing cavitation has been given by Arndt & Ippen (1967).

5. Some details of the cavitation dynamics deduced from high-speed motion photography

High-speed motion-picture photography, with frame rates ranging from 3000 to 8000 frames/s, was used to observe cavitation on both the tripped and the untripped hydrofoil. The cavitation was photographed along the span of the hydrofoil using back-lighting provided by a 2 kW 'colortran' lamp. The high-speed motion-picture camera was a Red Lake Laboratories Hycam model with a 400 ft film capacity and a 50 mm Schneider lens. Kodak high-speed Ektachrome (EFB 7242) 16 mm film was used for all movies. Both the camera and the lamp were situated outside the water tunnel with viewing through windows of commercial grade Plexiglas 2 in. thick. The distance from the inside wall of the tunnel viewing port to the centre of the hydrofoil was approximately 13 in. We shall discuss cavitation on the untripped hydrofoil first. The stroboscopic photographs in figures 4 and 6 will be used to illustrate the descriptions of the filmed observations.

For the untripped hydrofoil near inception, the film disclosed that small bubbles were generated at a location corresponding to the downstream extremity of the laminar separated flow region. This is illustrated in figures 4(*a*) and 8 (for which $\sigma \approx \sigma_i = 1{\cdot}15$) by the small cavitation bubbles at the location corresponding to the reattachment point. Following their formation, the bubbles moved forwards towards the location of $C_{p\min}$, stopping and joining at the leading edge of the separation zone to form a flattened single bubble, which is also shown in figures 4(*a*) and 8. Further generation of bubbles caused spanwise growth of each small bound cavity first along its downstream extremity and then along its leading edge. Eventually these smaller cavity regions joined adjacent ones. Concurrently, the height of the bound cavity as well as its chordwise extent increased, so that the bound cavitation region occupied a volume much larger than that probably occupied by the original, non-cavitating separation region. Figures 4(*a*) and (*b*), both obtained at $\sigma = \sigma_i$, show the mirror-like leading edge of the vapour pocket which was formed from the smaller bubbles. The downstream

section of the pocket is broken up, probably owing to turbulence in the liquid flow over it. Also, the larger extent of the fully developed cavity region compared with the incipient region is clearly evident. For the more advanced stages of cavitation, exemplified by figure 4(*c*), taken at $\sigma \approx 0{\cdot}74$, both the height and especially the chordwise length of the cavitation region grew and unsteadiness became apparent. Large three-dimensional quantities of bubbly mixture were ejected into the outer liquid liquid flow from the main bound cavitation region. Ejection occurring at the trailing edge of the bound cavitation region can be deduced in figure 4(*c*) from the spanwise non-uniformity of the trailing edge of the cavity region. The diameters of the bubbles in this mixture are estimated to be of the order of $\frac{1}{60}$ in. As the expelled two-phase mixture was carried downstream by the main flow, it continually changed shape and size and occasionally appeared to spin about an axis parallel to the span. The bubbles collapsed before reaching the trailing edge unless, as occurred at very low values of σ, the main cavity length was large. Occasionally a pocket of very small bubbles appearing as a cloud was swept downstream of the hydrofoil. These bubbles may have been gas-filled and their presence raises speculation that some gaseous diffusion had occurred within the main cavity region. The passage of the mixture downstream was often followed by clearly distinguishable, vertically oriented spinning groups of small bubbles (lower right corner of figure 4*c*). These bubbles often persisted downstream of the trailing edge. Their persistence and alignment indicated that they were trapped within the core of a strong vortex. At the spanwise edge of the main cavity region, recirculation of bubbles in the cavity was apparent.

These observations support the contention that inception on the untripped hydrofoil was caused by the flow separation as discussed in § 4. As the cavitation region grew with decreasing σ, the flow pattern of the outer, liquid phase was altered, causing unsteady turbulent separation at the downstream extremity of the cavity. An ejection process not unlike that occurring in and maintaining turbulent boundary layers existed. In the case of the turbulent boundary layer, Kline *et al* (1967), using dye injection in water, observed ejection of masses of dye-filled fluid from near the wall outwards into the mean flow followed by dye streaks nearly normal to the wall. In the current case, ejection of a bubbly volume followed by sweeping of bubble-filled vortices occurred. We can speculate that this process also occurs in the process of separation of non-cavitating turbulent boundary layers.

The high-speed motion picture of the tripped-hydrofoil cavitation showed clearly that separate events which involved the growth and the splitting of large single cavitation bubbles occurred. The film was made immediately after the tunnel had been filled with fresh water and subjected to a lengthy period of deaeration, so σ_i was abnormally low. The condition selected for filming was $\sigma = 0{\cdot}44$. At this index there was no observable water jet cavitation. Still photographs, however, were taken during previous acoustic measurements using a different tunnel filling, and some of these have been selected to illustrate observed trends of the filmed bubbles. At that time σ_i was higher than it was for the motion pictures. Two photographs which show examples of the events are given in figure 8 for $\sigma \approx 0{\cdot}91$ and in figure 6 for $\sigma = 0{\cdot}78$. Relatively near inception, represented by $\sigma = 0{\cdot}91$, where $\sigma_i = 1{\cdot}15$ (figure 8), bubbles began growing spherically, reaching maxima downstream of the point of $C_{p\min}$. A few of the bubbles were sufficiently far from the wall that they grew to a maximum size and then decreased in size, remaining nearly spherical. Nearer to the wall and probably inside

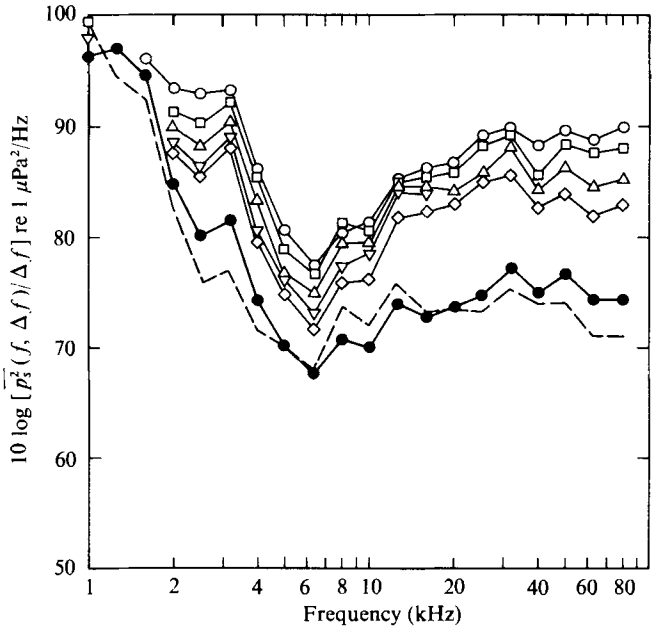

FIGURE 9. Spectral densities, referred to 1 yd, of sound generated by separation-induced cavitation for $U_\infty = 18$ ft/s, $\alpha = 4°$ and 10 % air content at atmospheric pressure. σ: ○, 0·64; □, 0·74; △, 0·84; ▽, 0·92; ◇, 1·02; ●, 1·15. Background with hydrofoil removed: – – –, $0{\cdot}6 \leqslant \sigma \leqslant 1{\cdot}15$.

the boundary layer, where the static pressures were lower, the bubbles grew to a larger size. When downstream of $C_{p\min}$ these bubbles had a prolate spheroidal shape with major axis normal to the plane of the hydrofoil. At their maximum sizes, the tips of the bubbles frequently touched the surface of the hydrofoil. While continuing to travel downstream, the bubbles developed varying degrees of local deformation at the point on their surface closest to the surface of the hydrofoil. A large number of bubbles which were formed close to the surface of the hydrofoil took on nearly hemispherical shapes that persisted until after they passed the point of $C_{p\min}$. At this point the liquid-phase flow over the bubbles apparently separated as in figure 6. That part of the bubble adjacent to the hydrofoil became stationary and the furthest part continued to move with the free stream. This caused stretching of the bubble, forming a two-phase mixture. The downstream extremity was an unbroken sector of the original bubble while the remainder of the mixture appeared to be a collection of small bubbles. As the stretching continued, the downstream extremity began to spin around a spanwise axis while the stretched portion consisted of two line filaments of small bubbles. It appeared that the large three-dimensional vortex generated by the separation split and entrained the bubble, so that while some vapour was carried by the free stream some was also bound to the hydrofoil. The collapse of these individual bubble systems began with the free vortex, followed by the small bubbles in the stretched vortex filaments, then the bubbles in the bound vortex on the hydrofoil. The small bubbles occurring in this cavitation were of the same apparent size as those occurring as a result of laminar separation.

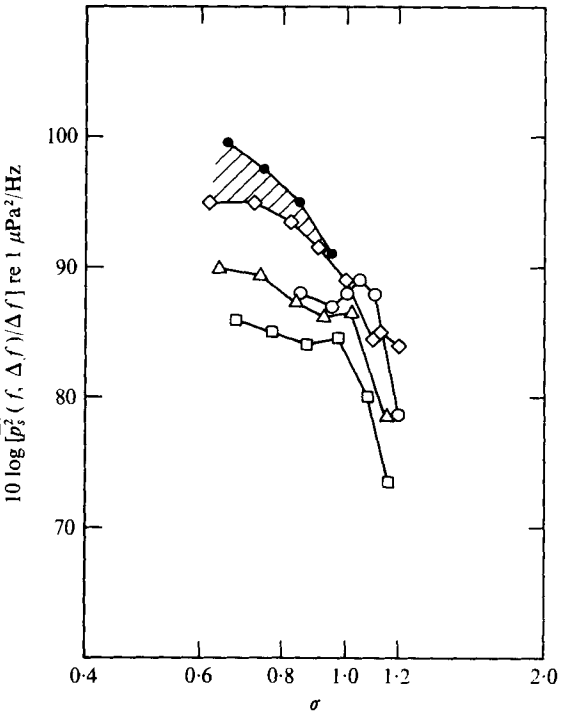

FIGURE 10. Sound spectral densities at 1 yd *vs.* cavitation index and water speed for the 31·5 kHz third octave frequency band. Spectra were obtained for no trip and $\alpha = 4°$. U_∞: ◇, 22 ft/s ($\sigma_i = 1{\cdot}12$); ●, 22 ft/s ($\sigma_i = 0{\cdot}97$); ○, 20 ft/s ($\sigma_i = 1{\cdot}12$); △, 18 ft/s ($\sigma_i = 1{\cdot}15$); □, 16 ft/s ($\sigma_i = 1{\cdot}08$).

6. Acoustic characteristics of the cavitation

The spectral densities of radiated sound from the untripped hydrofoil are shown in figure 9 for $U_\infty = 18$ ft/s and $\alpha = 4°$ for a range of σ. The spectral density has been referred to a 1 yd reference range by using the correction for tunnel reverberation. It is defined as

$$10 \log \overline{p_s^2}(f, \Delta f)/\Delta f,$$

where $\overline{p_s^2}(f, \Delta f)$ is the effective mean-square pressure at 1 yd measured in the $\frac{1}{3}$-octave bandwidth Δf at the frequency f. Below 2 kHz the background levels in the test section dominated the measurements. Above 6 kHz, the spectral density increased to a maximum near 31·5 kHz.† The spectrum levels for $\sigma = 1{\cdot}15$ are comparable to the background levels. Absorption effects accounted for an approximately 1 dB reduction in level near 50 kHz. The noise levels increased abruptly with the onset of cavitation and then continued to increase only slightly with a further reduction in cavitation index. The chordwise length of the major cavity region increased in extent from

† An additional peak at $f = 3{\cdot}15$ kHz is present in all spectra of noise yet it cannot be firmly explained by the results of the acoustic calibration. It is apparent from the calibration that discrete acoustic tunnel modes exist at this low frequency; these modes are expected on theoretical grounds. We speculate that the $f = 2{\cdot}5$ kHz and $f = 3{\cdot}15$ kHz bands are influenced by interaction of the bubbles with a discrete mode in this region. The test section is not considered reverberant below $f = 5$ kHz. This peak has also been observed in unpublished noise spectra from air-bubble emission.

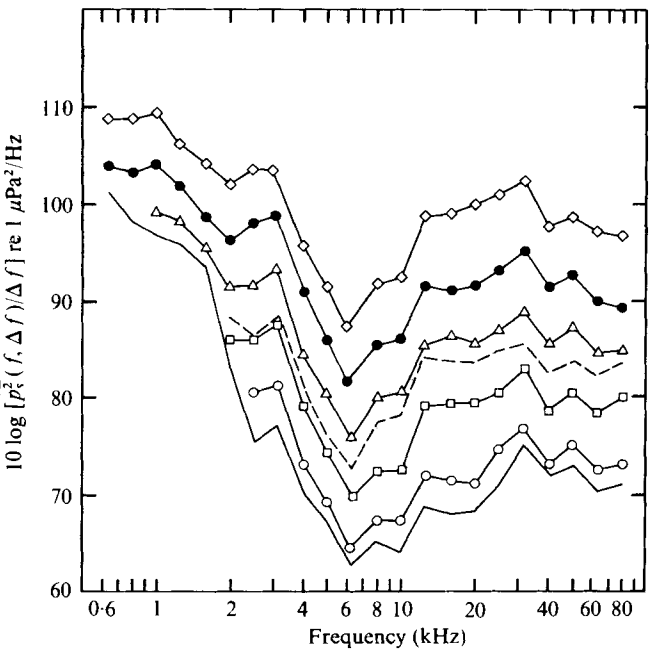

FIGURE 11. Spectral densities at 1 yd of travelling-bubble cavitation noise for various cavitation indices. Levels are for a tripped boundary layer at $U_\infty = 18$ ft/s, $\alpha = 4°$, $\sigma_i = 1{\cdot}15$ with 5 % air content at atmospheric pressure. σ (with trip): ◇, 0·80; ●, 0·90; △, 1·00; □, 1·10; ○, 1·20; ——, 1·30. σ (without trip): – – –, 0·92.

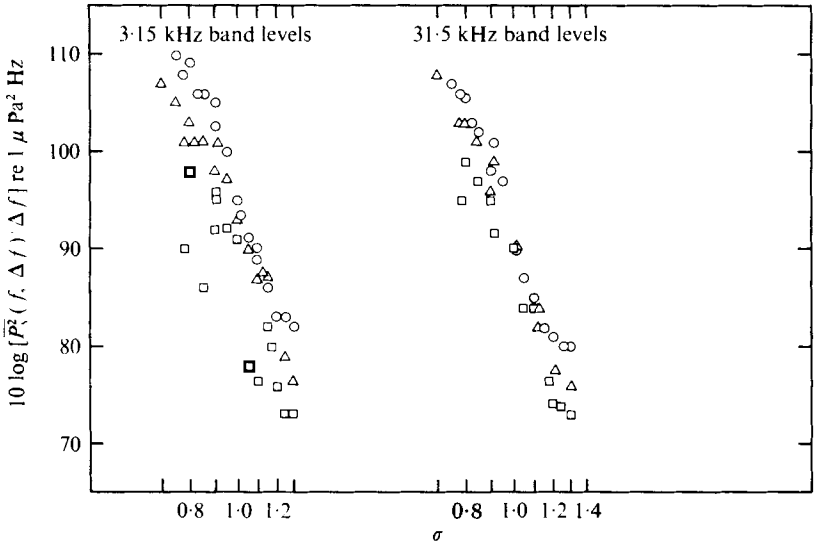

FIGURE 12. Dependence on cavitation index of spectral density levels at 1 yd for travelling-bubble cavitation noise at various speeds and $\alpha = 4°$. U_∞: ○, 22 ft/s ($\sigma_i = 1{\cdot}11$); △, 18 ft/s ($\sigma_i = 1{\cdot}12$); □, 16 ft/s ($\sigma_i = 1{\cdot}17$).

approximately $0{\cdot}25 < x/c < 0{\cdot}38$ at $\sigma = 0{\cdot}92$ to approximately $0{\cdot}25 < x/c < 0{\cdot}7$ at $\sigma = 0{\cdot}64$ ($\sigma_i = 1{\cdot}12$). For this increase in the extent of cavitation by a factor of 3, the noise levels increased by factors of approximately 5 at low frequencies and of 2 at frequencies near 30 kHz. The dependence of the noise levels at 31·5 kHz on σ for four water velocities is shown in figure 10. An abrupt increase in level for $\sigma < \sigma_i$ occurs for all speeds and reflects the rapid onset of cavitation. The sound levels in this band for constant $\sigma \simeq 0{\cdot}9$ increase roughly as $\overline{p_s^2}(f, \Delta f) \propto U_\infty^n$, with $n = 3$–4. The levels marked by filled symbols correspond to measurements obtained after a filling of the tunnel; those marked by open symbols were obtained after inception conditions had stabilized.

The cavitation noise for the tripped boundary layer is shown in figure 11. The general shapes of the spectral densities for this case are not unlike those of figure 9, but the levels are considerably higher. Near inception the dependence on σ is more gradual for the untripped hydrofoil. Although the tunnel possesses discrete modal properties for $f < 5$ kHz, we have applied the tunnel correction at low frequencies to give estimates of free-field sound. The gradual increase in sound level with reduction in σ is typical of all speeds, as shown in figure 12. There exists a speed dependence of the approximate form $\overline{p_s^2}(f, \Delta f) \propto U_\infty^n$, with $n = 3$–4, at a constant value of σ in the range $0{\cdot}8 < \sigma < 1{\cdot}0$.

Measured noise spectra for other angles of attack for both types of cavitation display similar dependences on σ and U_∞. In the case of travelling-bubble cavitation the gradual increase in the noise with a reduction in σ and the disappearance of intermittency indicated that a uniform increase in the number of available nuclei occurred. On the other hand, for the bound cavitation associated with laminar boundary-layer separation this was not the case. After inception and the abrupt onset of noise, mean-square low frequency sound pressure levels increased slightly more rapidly than the cavity extent and the high frequency levels slightly less rapidly. The high frequency levels of the spectra are peaked at nearly the same frequency for noise from each type of cavitation. An examination of a large number of enlarged stroboscopic photographs of each type of cavitation, however, disclosed that the diameters of the smallest bubbles in each case were of the order of $\frac{1}{80}$–$\frac{1}{60}$ in. It is plausible that the high frequency noise was controlled by the dynamics of these bubbles and this point will be further discussed in the next section. The process of bubble splitting by the liquid flow separation which was described in the previous section resulted in the small bubbles. The size distribution of these small bubbles was probably controlled by the length scale and intensity of the turbulence of the liquid flow. This phenomenon of splitting has been discussed by Sevik & Park (1972) in connexion with the splitting of air bubbles by turbulent water jets.

7. Dimensionless representations of the noise

The high-speed motion pictures of cavitation associated with the tripped boundary layer were used to generate behaviour patterns of the bubbles as a function of chordwise location. Figure 13 shows patterns for four of the bubbles which grew on the hydrofoil. The cavitation index was $\sigma = 0{\cdot}44$ and $U_\infty = 22$ ft/s. A total of twenty events (including both spherical and split bubbles) occurred in the 2 s film during which the sound level was measured. Figure 13 includes the history of a bubble which grew to a hemisphere and then was split by the flow separation around it at $x/c = 0{\cdot}4$. The other bubbles in figure 13 were spherical. Superimposed on the bubble diameters are

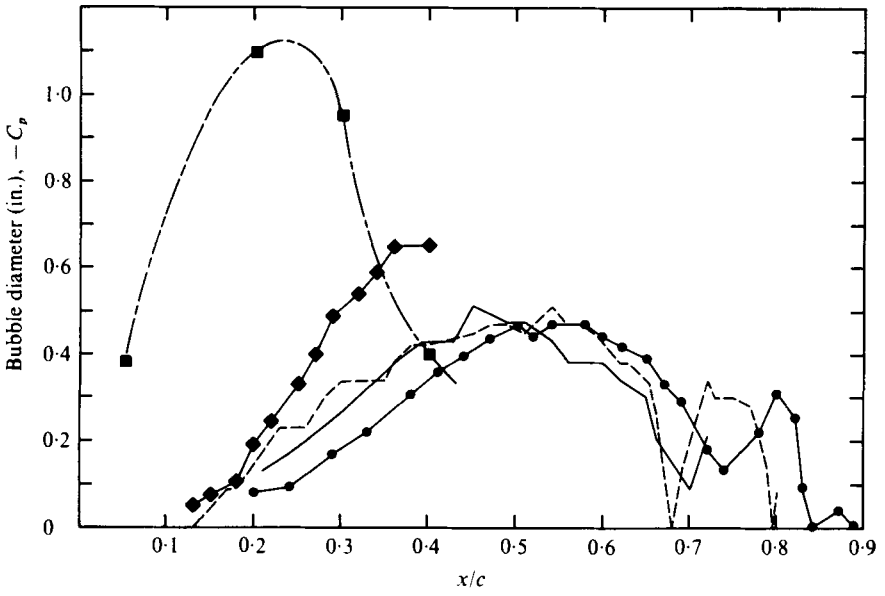

FIGURE 13. Filmed bubble histories for travelling-bubble cavitation compared with the measured pressure distribution on the tripped hydrofoil for $U_\infty = 22$ ft/s, $\sigma = 0{\cdot}44$, $\alpha = 4°$. ■, measured pressure coefficients; ◆, hemispherical bubble; ●—●, spherical bubbles.

the measured pressure coefficients from figure 3 as well as the best estimate of the pressure distribution. The continued growth of the bubbles downstream of $C_{p\min}$ is similar to that observed by Plesset (1949) on an axisymmetric head-form. In the present case one or two rebounds occurred. The maximum spherical-bubble radius can be estimated from Strasberg's (1956) approximate relationship

$$R_M = [\tfrac{1}{2}U_\infty^2(-\sigma - C_{p\min})]^{\frac{1}{2}}t', \tag{1}$$

where t' is the length of time that it takes for the bubble to pass through the region in which $p < p_v$. In our case

$$t' = l/U_\infty(1-\bar{C}_p)^{\frac{1}{2}}, \tag{2}$$

where l is the chordwise extent of this region ($l \simeq 0{\cdot}2c$) and $\bar{C}_p$ is the space-averaged static pressure coefficient there ($\bar{C}_p \simeq -0{\cdot}8$). Calculations using these equations overestimated the observed maximum bubble radii by approximately 20 %. Theoretical collapse times τ_0 for the bubbles, based on the theory of the empty bubble (Lamb 1945, p. 122), can be calculated from

$$\tau_0 = 0{\cdot}915R_M[\rho/(P_\infty - P_v)]^{\frac{1}{2}} = 0{\cdot}915\frac{R_M}{U_\infty}\left(-\frac{2}{\sigma}\right)^{\frac{1}{2}}. \tag{3}$$

Calculated values of τ_0 using observed R_M were less than observed collapse times by about 15 %.

These measurements of the travelling-bubble histories are used to non-dimensionalize the travelling-bubble cavitation noise of figure 11 on the basis of the observed dynamics of large bubbles in figure 13. The noise of a single spherical cavitation bubble has been shown by Fitzpatrick & Strasberg (1956) to have a frequency spectral density which is normalized as

$$S_b(f)\,r^2/R_M^4\rho P_\infty = S_b(f\tau_0). \tag{4}$$

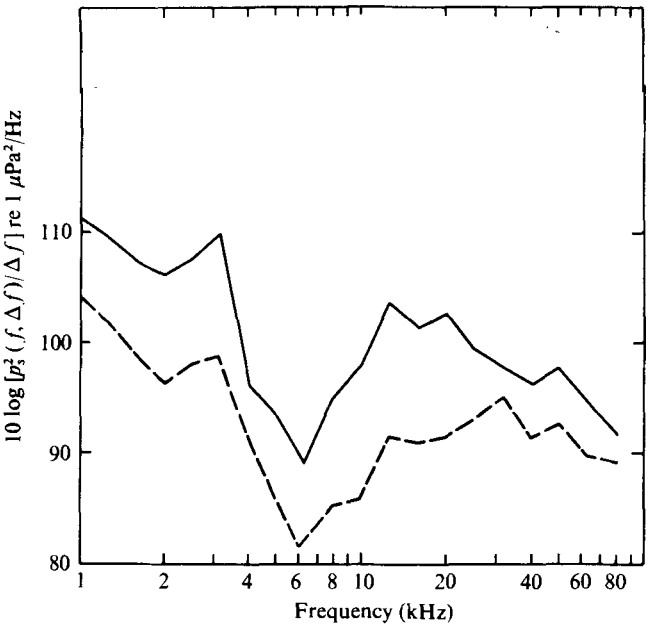

FIGURE 14. Spectral densities at 1 yd for travelling-bubble cavitation. ——, noise spectrum obtained during filming of bubbles in figure 13, $\sigma = 0{\cdot}44$, $U_\infty = 22$ ft/s; – – –, spectrum from figure 11, $\sigma = 0{\cdot}9$, $U_\infty = 18$ ft/s.

Here r is the acoustic range of the noise and the spectrum is defined such that

$$\int_0^\infty S_b(f)\,df = \int_0^\infty p_b^2(t)\,dt = \gamma\tau_0\overline{p_0^2},$$

where $\gamma\tau_0$ is the total lifetime of the bubble (including growth, initial collapse times and rebounding times) expressed in multiples of τ_0 and where $p_b(t)$ is the sound level from the single-bubble motion and $\overline{p_b^2}$ is its time-averaged mean square. A measured sound pressure level in a narrow frequency band Δf can be interpreted as a similar spectrum

$$S(f) = \gamma\tau_0\overline{p_s^2}(f, \Delta f)/\Delta f, \tag{5}$$

where $\overline{p_s^2}(f, \Delta f)$ is the measured mean-square pressure in the filter band. From the bubble dynamics filmed in the current study we find that $\gamma \simeq 3$; this value of γ is the same as that used by Fitzpatrick & Strasberg (1956). The spectral density of the sound generated by the bubbles in figure 13 is shown in figure 14. Note that compared with the levels at high frequency in figure 11 for $\sigma = 0{\cdot}8$ and $0{\cdot}9$ the peak levels for $\sigma = 0{\cdot}44$ occur at a lower frequency. Normalization of data from figure 11 as well as from figure 14 gives the spectra shown in figure 15 in the dimensionless form analogous to (4):

$$S(\tau_0 f) = \frac{\overline{p_s^2}(f, \Delta f)}{\Delta f}\frac{\gamma\tau_0 r^2}{R_M^4 \rho P_\infty}. \tag{6}$$

Values of R_M were determined from (1) and values of τ_0 from (2). Note that the peak in the high frequency spectrum for $\sigma = 0{\cdot}44$ and $U_\infty = 22$ ft/s now corresponds more closely with that for $\sigma = 0{\cdot}9$ and $U_\infty = 18$ ft/s than it did when it was not normalized.

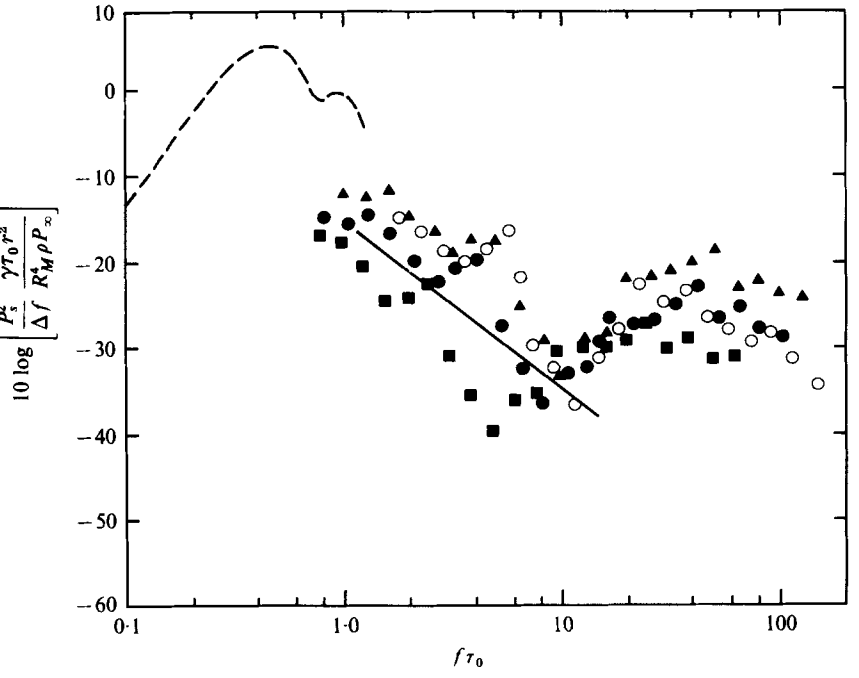

FIGURE 15. Dimensionless spectral densities for various conditions of travelling-bubble cavitation. Normalization is based on variables associated with single-bubble cavitation noise. ▲, $\sigma = 0{\cdot}8$, $U_\infty = 18$ ft/s; ●, $\sigma = 0{\cdot}9$, $U_\infty = 18$ ft/s; ■, $\sigma = 1{\cdot}0$, $U_\infty = 18$ ft/s; ○, $\sigma = 0{\cdot}44$, $U_\infty = 22$ ft/s; – – –, theoretical values of Fitzpatrick & Strasberg.

We can compare the measured dimensionless sound spectrum with that computed by Fitzpatrick & Strasberg for ideal single-bubble motions by noting the similarity between (4) and (6). To this end we assume that the measured pressure $\overline{p_s^2}(f, \Delta f)$ is due to a sum of sound pressures occurring independently at a rate N per second, so that the dimensionless spectral density is

$$S(\tau_0 f) = N\tau_0 \gamma S_b(\tau_0 f),$$

where $S_b(\tau_0 f)$ is Fitzpatrick & Strasberg's (1956) spectrum for single-bubble cavitation noise. For purposes of comparison with measurements we shall assume a rate of one event involving a single spherical bubble per second although the photographs of the actual cavitation disclose a more complex composition of bubble motions. Figure 15 shows that the theoretical spectral density of the sound is greater than those which were measured. It also shows that the reported low frequency limit of the noise measurement did not include effects of the growth stage of the bubble motions. These dynamics are responsible for noise in the frequency range $f\tau_0 < 1{\cdot}0$.

The spread in the normalized data in figure 15 demonstrates that the non-dimensionalization in figure 15, being based on a presumed sequence of independent bubble events, does not fully account for the statistics of bubble collapses. This is indicated by the spread of dimensionless spectrum levels. We interpret the higher dimensionless levels at $\sigma = 0{\cdot}8$ for $U_\infty = 18$ ft/s compared with those at $\sigma = 1{\cdot}0$ at the same speed as being related to a higher rate of bubble events at the lower cavitation index. As

discussed in § 4, the cavitation noise became less intermittent as σ decreased below σ_i and this suggests that a larger number of nuclei became available as cavitation sites. These aspects of the scaling and the modelling of event rates have been examined by Baiter (1974), who points out many uncertainties in the establishment of event rates. Apart from the unknown distributions of nuclei, Il'ichev & Lesunovskii (1963) show that the probability distribution of events can depend on the statistical nature of turbulence in the flow. Furthermore, when multiple events occur simultaneously it is not clear that the total radiated power from the ensemble is the linear sum of the powers from individual events because of bubble interactions.

Turning now to the shape of the spectral density for $f\tau_0 > 1{\cdot}0$, we note that the high-speed photography indicated the existence of a ratio of large to small bubble sizes of the order of 50. A translation of the theoretical noise peak from $f\tau_0 = 0{\cdot}5$ to $f\tau_0 = 25$ to account for the characteristic collapse time (which is proportional to bubble radius) of the smaller bubbles causes the theoretical peak to correspond roughly to that in the dimensionless spectrum of figure 15. In the range $1 < f\tau_0 < 10$ the dependence $(f\tau_0)^{-2}$ roughly fits the trend of the data. Unfortunately the peak at $f = 3{\cdot}15\,\mathrm{kHz}$ distorts this frequency dependence. A similar dependence has been observed by Jorgensen (1961) for noise from cavitating jets and by Mellen (1954) for noise produced by cavitation at the tip of a rotating rod. Fitzpatrick & Strasberg (1956) and more recently Baiter (1974) have suggested that this frequency dependence is associated with the influence of compressibility of the water.

We point out that the peak sound pressure occurring at $U_\infty = 18\,\mathrm{ft/s}$, $\alpha = 4°$ and $\sigma = 0{\cdot}74$ was in the range

$$|p_s|\, r/R_M P_\infty \simeq 4.$$

It is curious that this value is only one-tenth of that observed by Harrison (1952) for single cavitation bubbles, which were formed either in a venturi or by a spark.

The dimensionless form of the measured sound spectrum given by (6) can be rewritten in terms of flow variables by using (1)–(3). Substitution gives the equivalent form

$$S(\tau_0 f) = \frac{\overline{p_s^2}(f, \Delta f)}{\Delta f} \frac{U_\infty/c}{(\frac{1}{2}\rho U_\infty^2)^2[\sigma(\sigma_i - \sigma)]^{1{\cdot}5}} \left\{2\gamma \left(\frac{r}{c}\right)^2 \left(\frac{c}{l}\right)^3 [1 - \bar{C}_p]^{1{\cdot}5}\right\}. \tag{7}$$

The term in curly brackets is a constant which is characteristic of the hydrofoil, and is numerically equal to $1{\cdot}8 \times 10^5$ for the hydrofoil examined. The other factors depend on the operation variables. In these terms, the non-dimensionalization has a more general significance which may be applied to the other type of cavitation on the hydrofoil. This definition of $S(\tau_0 f)$ was applied to the spectrum of noise from the hydrofoil without tripping and the dimensionless result is shown in figure 16. The dimensionless frequency is

$$f\tau_0 = \frac{fc}{U_\infty} \frac{l}{c} \left[\frac{\sigma_i - \sigma}{\sigma(1 - \bar{C}_p)}\right]^{\frac{1}{2}}. \tag{8}$$

A comparison of this dimensionless spectrum with that in figure 15 shows more clearly that travelling-bubble cavitation noise is greater than that generated by bound cavitation. Also, we note that, for $\tau_0 f < 10$, the noise spectra in figure 16 are more adequately described by the dimensionless grouping of (7) than are the noise spectra in figure 15.

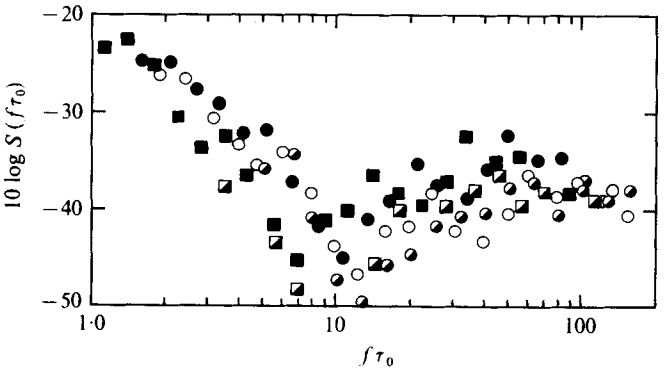

FIGURE 16. Dimensionless spectral densities of cavitation noise from the untripped hydrofoil calculated using (7) and (8).

	■	○	●	◕	◪
U_∞ ft/s)	22	16	22	18	18
σ	0·91	0·77	0·72	0·74	0·74
σ_i	1·12	1·11	1·12	1·15	1·15

8. Summary

The noise from bound cavitation has been demonstrated, for the hydrofoil examined, to be dependent on viscous effects in the form of changes in the boundary layer. When laminar boundary-layer separation occurred, considerable noise was produced at high frequencies, probably by the formation of small bubbles. These bubbles were carried in groups within long vortex filaments which were ejected into the non-cavitating free stream from the bound cavity. At a given speed, the bound cavity increased in size as the cavitation coefficient decreased, and after the inception of cavitation radiated sound levels increased slowly with further decreasing cavitation index. An increase in the extent of cavitation caused a nearly proportional increase in the acoustic mean-square pressure.

When laminar separation was eliminated by tripping the boundary layer into turbulence, inception was delayed and travelling-bubble cavitation occurred. For this type of cavitation, the magnitude of the noise was generally greater than that produced by bound cavitation due to separation. The noise mechanism was complicated by local flow separation around those bubbles closest to the surface of the hydrofoil. This caused the disintegration of large hemispherical bubbles into restricted collections of smaller ones causing high frequency noise. Large bubbles which were suitably far from the hydrofoil surface maintained a nearly spherical shape during growth and collapse and produced low frequency noise. This noise was estimated from theoretically determined single-bubble cavitation noise spectra. The dependence of the measured noise on the cavitation index after inception was much greater than for cavitation associated with laminar separation. For travelling-bubble cavitation, a continued reduction in cavitation index introduced a larger number of nearly independent bubble events and these caused increasing levels of noise. A marked difference between the two cavitation types in the dependence of noise on cavitation index was thus observed.

In comparing the noise radiated by the two types of cavitation we note that, since inception was slightly delayed by tripping, the onset of noise was also delayed. How-

ever, even though inception was delayed the noise actually exceeded the separation-induced cavitation noise by several dB in the more advanced stages of travelling-bubble cavitation. We speculate that this is the combined effect of more statistically independent events in the latter case as well as more gaseous diffusion brought about by long residence times in the cavity zone in the untripped case. Both the noise and the inception results have raised speculation that changes in nucleus content could affect different types of cavitation in different ways, viz. travelling-bubble compared with bound cavitation.

A simple scaling of the cavitation noise spectra was probably limited by the unknown dependence of event rates on flow variables as well as the uncertainty in the physical quantities affecting the small bubbles. Although it has been speculated that these bubbles were generated by the splitting of large ones by turbulent separation we have not yet quantified the flow variables which control the process.

The authors appreciate helpful discussions with Dr M. Sevik and Dr M. Strasberg concerning aspects of bubble and cavitation dynamics and with Dr F. Peterson concerning viscous effects on cavitation inception. We also appreciate the contribution of Dr H. Wang in assessing the hydrofoil pressure distributions and thank Mr George Lindstrom for the stroboscopic photographs, The work was sponsored by the David W. Taylor Naval Ship Research and Development Center In-House Independent Research Program.

REFERENCES

ACOSTA, A. J. 1974 Cavitation and fluid machinery. *Cavitation Conf., Edinburgh, Scotland.*

ARAKERI, V. H. 1974 A note on the transition observations on an axisymmetric body and some related fluctuating wall pressure measurements. *J. Fluids Engng, Trans. A.S.M.E.* **97** (1), 82–86.

ARAKERI, V. H. & ACOSTA, A. J. 1973 Viscous effects in the inception of cavitation on axisymmetric bodies. *J. Fluids Engng, Trans. A.S.M.E.* **95** (1), 519–528.

ARNDT, R. E. A. & IPPEN, A. T. 1968 Rough surface effects on cavitation inception. *J. Basic Engng, Trans. A.S.M.E.* **90**, 249–261.

BAITER, H. J. 1974 Aspects of cavitation noise. *Symp. High Powered Propulsion of Large Ships, Wageningen.*

BLAKE, W. K. 1975 Statistical description of pressure and velocity fields at trailing edges. *Naval Ship R. & D. Center Rep.* no. 4241.

BLAKE, W. K., WOLPERT, M., GEIB, F. & WANG, H. 1976 Acoustic radiation from cavitation on a thick hydrofoil. *Naval Ship R. & D. Center Rep.* no. 76–0051.

BROCKETT, T. 1972 Some environmental effects on headform cavitation inception. *Naval Ship R. & D. Center Rep.* no. 3974.

CASEY, M. V. 1974 The inception of attached cavitation from laminar separation bubbles on hydrofoils. *Cavitation Conf., Edinburgh, Scotland.*

FITZPATRICK, H. & STRASBERG, M. 1956 Hydrodynamic sources of sound. *2nd Symp. Naval Hydrodyn., Washington, D.C.* pp. 241–280.

HALL, D. J. & GIBBINGS, J. C. 1972 The influence of stream turbulence and pressure gradient upon boundary layer transition. *J. Mech. Engng Sci.* **14**, 134–146.

HARRISON, M. 1952 An experimental study of single bubble cavitation noise. *D.T.M.B. Rep.* no. 815.

HOLL, J. W. 1960 An effect of air content on the occurrence of cavitation. *J. Basic Engng, Trans. A.S.M.E.* **82**, 941–946.

HOLL, J. W., ARNDT, R. E. A. & BILLET, M. L. 1972 Limited cavitation and the related scale effects problem. *2nd Int. Japan Soc. Mech. Engrs Symp.*

Il'ichev, V. I. & Lesunovskii, V. P. 1963 On the noise spectra associated with hydrodynamic cavitation. *Sov. Phys. Acoustics* **9**, 25–28.

Jorgenson, D. W. 1961 Noise from cavitating submerged water jet. *J. Acoust. Soc. Am.* **33**, 1334–1338.

Kline, S. J., Reynolds, W. C., Schraub, F. A. & Runstadler, P. W. 1967 The structure of turbulent boundary layers. *J. Fluid Mech.* **30**, 741–773.

Knapp, R. T., Daily, J. W. & Hammett, F. G. 1970 *Cavitation*. McGraw-Hill.

Lamb, H. 1945 *Hydrodynamics*. Dover.

Liebeck, R. H. 1973 A class of airfoils designed for high lift in incompressible flow. *J. Aircraft* **10**, 610–617.

Mellen, R. H. 1954 Ultrasonic spectrum of cavitation noise in water. *J. Acoust. Soc. Am.* **26**, 356–360.

Peterson, F. B. 1969 Water tunnel-high speed basin cavitation inception comparison. *12th Int. Towing Tank Conf.* pp. 519–523.

Peterson, F. B. 1972 Hydrodynamic cavitation and some considerations of the influence of free-gas content. *9th Symp. Naval Hydromech., Paris.*

Plesset, M. S. 1949 The dynamics of cavitation bubbles. *J. Appl. Mech., Trans. A.S.M.E.* **16**, 277–282.

Schlichting, H. 1960 *Boundary Layer Theory*. McGraw-Hill.

Sevik, M. & Park, S. H. 1972 The splitting of drops and bubbles by turbulent fluid flow. *J. Basic Engng, Trans. A.S.M.E.*, paper 72WA/FE-32, pp. 1–8.

Strasberg, M. 1956 The influence of air-filled nuclei on cavitation inception. *D.T.M.B. Rep.* no. 1078.

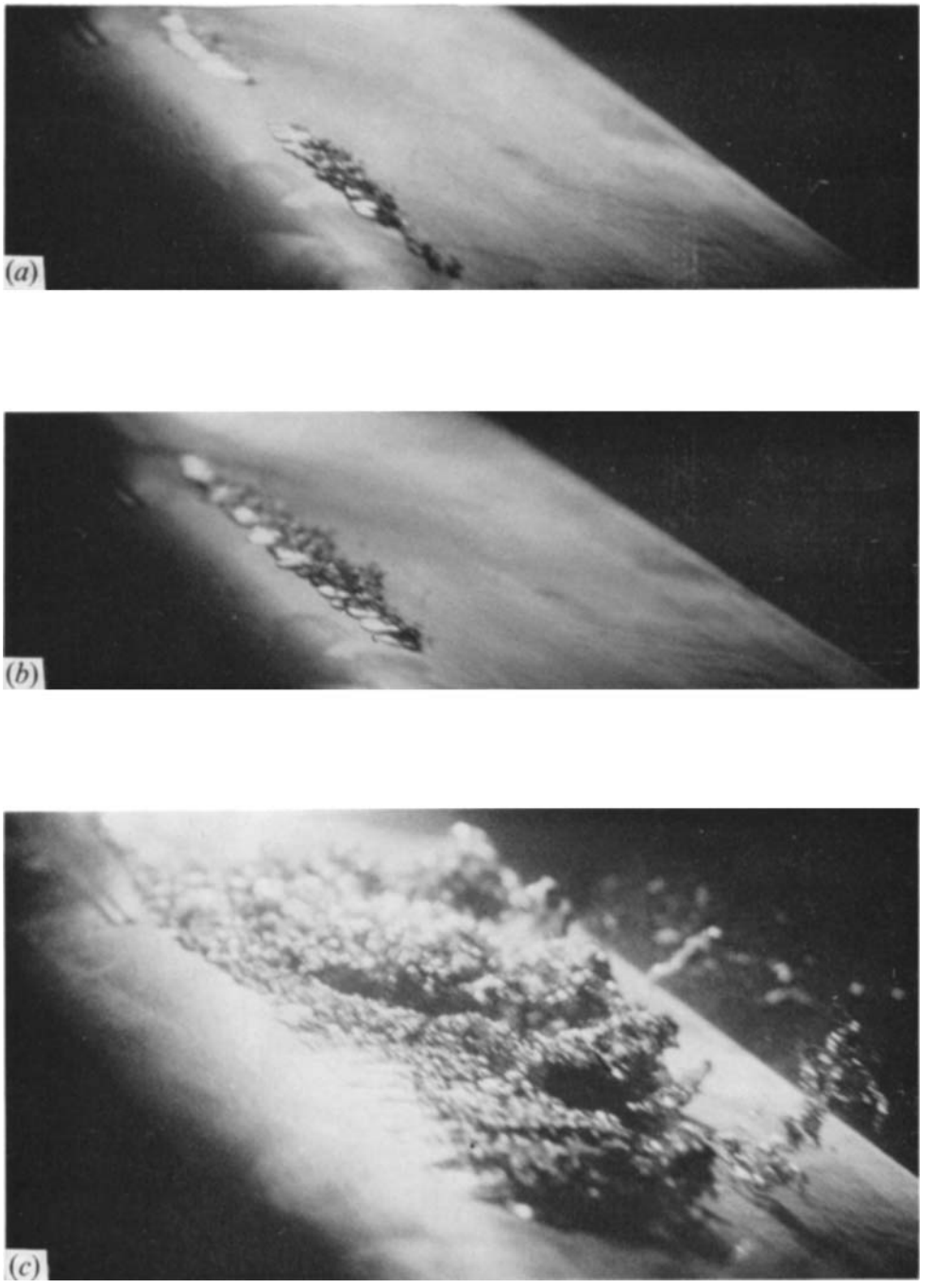

FIGURE 4. Representative photographs of cavitation without boundary-layer tripping. (*a*), (*b*) $\sigma = 1{\cdot}15$ with $U_\infty = 16$ ft/s. (*c*) $\sigma = 0{\cdot}74$ with $U_\infty = 20$ ft/s.

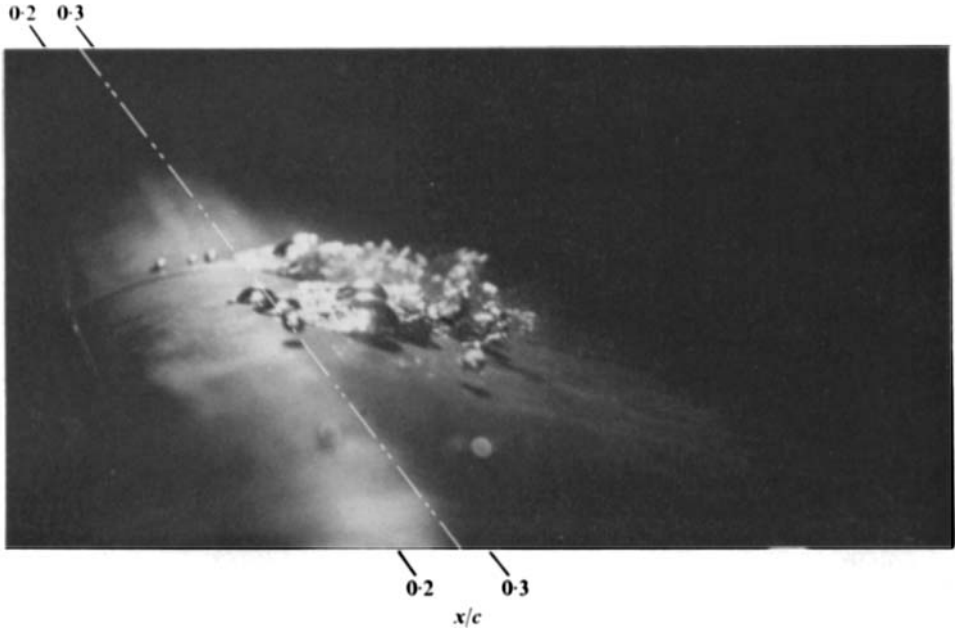

FIGURE 6. Travelling-bubble cavitation associated with the tripped turbulent boundary layer for $U_\infty = 22\,\text{ft/s}$, $\alpha = 4°$, $\sigma = 0{\cdot}78$ and $\sigma_i = 1{\cdot}15$. ——·——, $C_{p\min}$ (calculated).

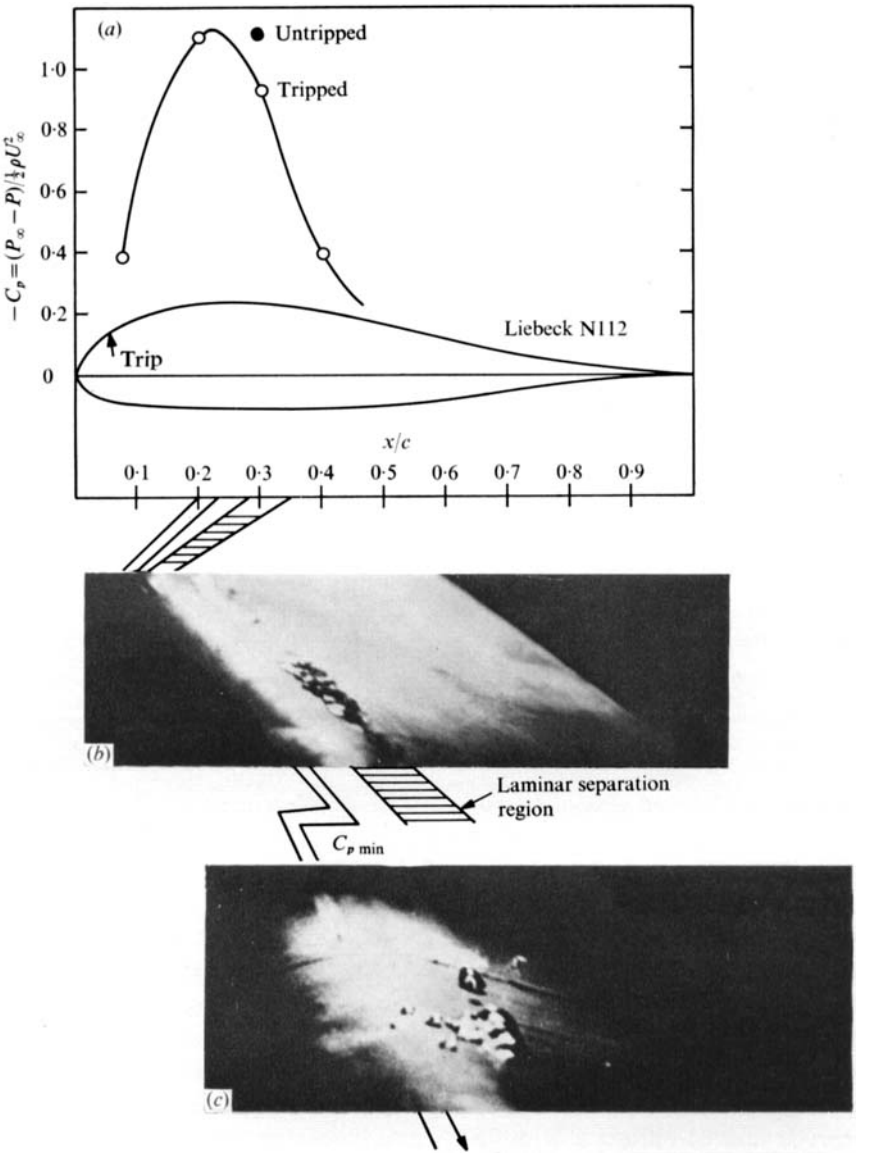

FIGURE 8. (*a*) Diagram showing the pressure distributions and cavitation patterns near inception as influenced by viscous effects. (*b*), (*c*) Photographs obtained at differing angles to optimize lighting; lines mark co-ordinates of $x/c = 0{\cdot}2$, the location of $C_{p\min}$ and the observed separation zone. (*b*) Laminar separation (untripped), $U_\infty = 16$ ft/s. (*c*) Turbulent boundary layer (with trip), $U_\infty = 18$ ft/s.